



Effects of latent heat in various cloud microphysics processes on autumn rainstorms with different intensities on Hainan Island, China

Jiangnan Li ^{a,*}, Kailu Wu ^a, Fangzhou Li ^a, Youlong Chen ^b, Yanbin Huang ^b, YeRong Feng ^c

^a School of Atmospheric Sciences, Sun Yat-Sen University, Guangzhou 510275, PR China

^b Hainan Meteorological Service, Haikou 570203, PR China

^c Guangdong/CMA Key Laboratory of Regional Numerical Weather Prediction, Guangzhou 510080, PR China



ARTICLE INFO

Article history:

Received 24 October 2016

Received in revised form 2 January 2017

Accepted 18 January 2017

Available online 25 January 2017

Keywords:

Autumn rainstorm

Hainan Island

Latent heat

Cloud microphysics

ABSTRACT

In this study, we used the Weather Research and Forecasting (WRF) and WRF-3DVAR models to perform a series of simulations of two autumn rainstorms on Hainan Island. The results of neighborhood fractions and Hanssen skill scoring (FSS, HSS) methods show that the control experiments reproduced well two heavy rainfall episodes. Effects of latent heat in various cloud microphysical processes are different at distinct intensities or stages of precipitation. In the absence of any heating effect of deposition, precipitation weakened. The greater was the precipitation, the more significant was the weakening effect. Ascending movement at upper troposphere could be weakened or descending movement at lower troposphere enhanced. With decreases in the strength of precipitation, cloud ice, snow, graupel, and rainwater, increases in latent heat lessened. With weak precipitation, at upper troposphere the rainwater content increased and snow and ice content decreased, whereas at middle troposphere, the ice, snow, and graupel contents increased. Latent heating increased at middle and lower troposphere and decreased at upper troposphere. The absence of any heating effect of freezing had little effect on precipitation. By removing the evaporative cooling of cloud water, the interactions between vertical movement and cloud microphysical processes resulted in a weakening of strong precipitation and an intensification of weak precipitation. However, in the preliminary stages of these two precipitation events, snow, graupel, cloud ice, and rainwater all increased, and precipitation was enhanced in both. In the later stages, strong precipitation systems weakened and weak precipitation systems strengthened. Latent heating first increased and then dropped in strong precipitation systems, whereas they continuously increased in weak precipitation systems.

© 2017 Elsevier B.V. All rights reserved.

1. Introduction

In the Golden Week of China's National Day (October 1st) in 2010 and 2011, continuous rainstorms occurred on the island province of Hainan, causing human casualties and great properties losses and significantly impacting the tourism industry. Hainan's geographical location is unique, being located in the South China Sea (SCS) with high mountainous ground in the island center and lower lands all around. October is the SCS summer monsoon withdrawal period, and the causes of rainstorms are complex. Cloud microphysical processes play an important

role in the development and evolution of cloud, precipitation and weather systems. First, the phase transition processes between hydrometeors in clouds that either directly release or absorb latent heat affect the vertical structure of the atmosphere. Secondly, descending hydrometeors will generate a drag effect, which directly impacts the strength and distribution of the ascending airflow. Thirdly, cloud microphysical processes can affect land-surface processes. Fourthly, cloud particles can absorb, scatter, and reflect radiation and influence the energy balance. Due to limitations in detection technology, numerical modeling is frequently used to explore cloud microphysical processes (e.g., Sui et al., 2005; Zhu and Zhang, 2006; Rogers et al., 2007; Li and Pu, 2008; Tao et al., 2011; Li et al., 2013a, 2013b; Li and Shen, 2013; Fernández-González et al., 2016; Jiang et al., 2016; Huang and Wang, 2017). Because of the different precipitation mechanisms associated with different seasons, regions, geographical environments, and

* Corresponding author.

E-mail address: essljn@mail.sysu.edu.cn (J. Li).

weather systems, many kinds of microphysics schemes have been proposed. Most researches have focused on individual cases and the conclusions are not necessarily applicable to other cases. Huang and Wang (2017) showed that hydrometeors over the Pacific warm pool have unique microphysical processes relating to their development and depletion. Hence, a better understanding of the cloud microphysical properties of autumn rainstorms in Hainan would be an important contribution.

Through mesoscale and cloud-scale models, most works aim to develop a deeper understanding of cloud microphysical processes (e.g., Jankov et al., 2005, 2007; Zhu and Zhang, 2006; Gao et al., 2006; Rogers et al., 2007; Thompson et al., 2008; Rosenfeld et al., 2012; Lin et al., 2011; Li et al., 2013a, 2013b; Guo et al., 2015; Fernández-González et al., 2016; Sarkadi et al., 2016; Huang and Wang, 2017). Previous researches have had two main focuses: the first has been to gain knowledge about the cloud microphysical processes of typhoons or summer rainstorms (e.g., Zhu and Zhang, 2006; McFarquhar et al., 2006; Patnaik and Krishnamurti, 2007; Rogers et al., 2007; Li and Pu, 2008; Lin et al., 2011; Tao et al., 2011; Li et al., 2013a, 2013b; Jiang et al., 2016) and most of these studies have involved a comparison of sensitivity test results of various microphysical schemes. In general, the study results have indicated that microphysics schemes do not greatly influence a typhoon's track, but do affect its intensity and structure. Secondly, researchers have sought to improve cloud microphysical schemes to more accurately analyze parameterization calculations for certain hydrometeors (e.g., Thompson et al., 2004; Straka and Mansell, 2005; Thompson et al., 2008; Dudhia et al., 2008; Adams-Selin et al., 2013; Morrison and Milbrandt, 2015; Barthe et al., 2016). For example, Adams-Selin et al. (2013) used the Weather Research and Forecasting (WRF) model to study the effect of graupel size and descending final velocity on precipitation. The authors found that larger size and greater falling velocity leads to more precipitation. Barthe et al. (2016) showed that graupel fall speeds can influence the occurrence of lightning flashes in tropical cyclones.

Cloud microphysical processes include phase transformation and temperature change in hydrometeors, which can cause latent heating or cooling, and thereby affect the vertical structure of the atmosphere and dynamic field (e.g., Zhang, 1989; Tao and Simpson, 1989; Yin et al., 2000; Levin et al., 2005; Flossmann and Wobrock, 2010; Li and Shen, 2013; Adams-Selin et al., 2013; Guo et al., 2015; Fernández-González et al., 2016; Sarkadi et al., 2016; Huang and Wang, 2017). Zhang (1989) used a mesoscale static model to simulate the June 1977 Johnstown floods in the United States and found that growth in condensation and deposition favored the development of a middle-level warm center. In their simulation of a tropical squall line, Tao and Simpson (1989) found different main microphysical processes of precipitation in a convective region and a stratiform cloud area and

that the main processes in the precipitation maturation and extinction phases differed as well. Wang (2002) discovered that the evaporation of rainwater and the melting of snow and graupel play a vital role in the generation of tropical cyclonic rain bands and sinking airflow. Colle et al. (2005) found that condensation, melting, deposition of snow, and collection of cloud water by rainwater were important microphysical processes in orographic rain. Wang et al. (2010) and Shen et al. (2011a, 2011b) stated that the influence of cold cloud on precipitation was more significant than the influences of vertical wind shear and radiation in South China precipitation prior to the flood season. The authors found that cloud ice collected by snow and snow collected by graupel were the critical microphysical processes during the development of cold cloud. Using a 2-D cloud model, Li and Shen (2013) investigated the rain microphysical processes in tropical deep convection. Huang and Wang (2017) showed that liquid-phase hydrometeors dominate the evolution of thunderstorms over the Pacific warm pool.

The focus of the above studies was the overall effect of a certain microphysical process and most related to typhoon or rainstorm in summer. However, each cloud microphysical process is associated with many influence factors and there are also a variety of parameter calculation methods. In this study, we focus on the impacts of latent heating (or cooling) in various cloud microphysical processes on autumn rainstorms with different intensities on Hainan.

This paper is organized as follows. An overview of the case studies is described in Section 2. In Section 3, we describe our experimental design. In Section 4, we verify the results of our control experiment. We perform a comparative analysis of the results of three sensitivity experiments in Section 5 and we summarize in Section 6.

2. Overview of individual cases of rainstorm

2.1. Case A

The nine-day rainstorm from September 30 to October 09, 2010 in Hainan was the longest duration of heavy rain since 1961. The average precipitation over the whole island reached 648.3 mm—six times higher than the average of the same period from 1951 to 2009 (93.1 mm). From the time meteorological recordkeeping began in Hainan in 1951, the maximum daily precipitation ever recorded (881.8 mm) at a single station occurred in Boao town, Qionghai City on October 5. With its nine day duration, this rainstorm also broke the record for the maximum duration of a continuous rainstorm. The direct economic losses totaled 13.4 billion dollars.

Judging from the 500 hPa circulation field (Fig. 1), Hainan was in the south of the area with a subtropical high from September 29 to October 2, and east wind prevailed. There was a tropical disturbance in the region of 5°N–15°N, 95°E–100°E. The upper-air chart of October 5 showed

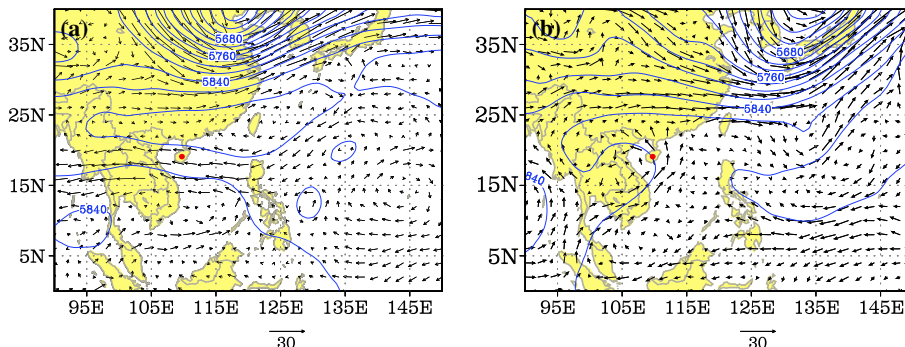


Fig. 1. Wind (black arrow, unit: m/s) and geopotential height (blue line, unit: gpm) at 500 hPa at (a) 1200 UTC 2 Oct; (b) 0000 UTC 5 Oct 2010. Red filled circle indicates location of Hainan Island.

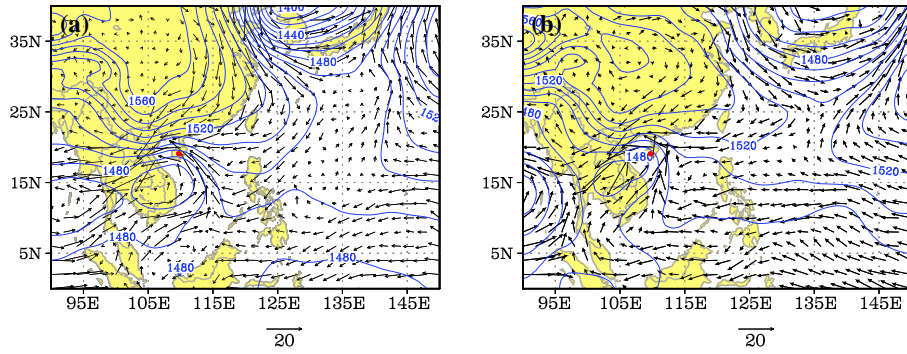


Fig. 2. Wind (black arrow, unit: m/s) and geopotential height (blue line, unit: gpm) at 850 hPa at (a) 1800 UTC 3 Oct; (b) 0000 UTC 5 Oct 2010. Red filled circle indicates location of Hainan Island.

that this subtropical high had retreated and was pressing southward, while the tropical disturbance moved eastward and northward. Therefore, Hainan controlled the southeast airflow of the tropical disturbance.

Based on the 850 hPa circulation field (Fig. 2), the cross-equator southwesterly airflow strengthened its northward movement, and there was a tropical anticyclone in the south of the tropical depression area. The north was controlled by a continental cold high and the east was influenced and controlled by a subtropical high, thus forming a circulation pattern with one low-pressure area and three high-pressure areas. On October 3, the equatorial anticyclone moved northward to the region of 5°N–10°N, 95°E–100°E and continued to maintain that direction, which was conducive to the development and movement of the tropical depression. On October 5, the southeast jet stream on the periphery of the tropical depression converged with the east jet stream in northeastern Hainan. On the night of October 6, the equatorial anticyclone died out, and the lower troposphere southwest jet stream weakened and disappeared. The tropical depression system also entered the dissipating stage.

2.2. Case B

Influenced by Typhoon Nalgae from 0000 UTC October 01, 2011 to 0000 UTC 8 October, the total precipitation in Haikou city reached 683 mm. Within the 24 h from 1200 UTC 4 October, the precipitation in Haikou base station reached 333.6 mm, which was also the maximum ever recorded from the time meteorological recordkeeping began in Haikou in 1951.

The 500 hPa upper-air chart (Fig. 3) shows that the subtropical high remained stable around 25° N, but the position of its western ridge point vacillated, repeatedly moving eastward and westward. With the sudden eastward movement of the western ridge point, the coverage of the typhoon expanded, whereas it would otherwise have narrowed. At 1200 UTC 4 October, southeast wind prevailed in Hainan due to the impact of “Nalgae” and the subtropical high. The 850 hPa flow field (Fig. 4) indicated that the cyclonic circulation moved northeastward; it was located in Hainan at 0600 UTC 4 October and began moving toward the Beibu Gulf at 1200 UTC 4 October. At this time, the southeast jet stream converged with the east jet stream in the periphery of the depression at the northern coast of Hainan. At 1200 UTC 5 October, the cyclonic circulation was located over eastern Vietnam and conditions in Hainan were controlled by the east jet stream.

Both rainstorms were caused by a low-altitude southeast jet stream, east jet stream, and southward-moving cold air. In the 2010 rainstorm, these three airflows converged in northeastern Hainan, whereas in 2011 they converged in the Beibu Gulf.

3. Experiment design

The WRF-ARW (version 3.4) model (Skamarock and Klemp, 2008) was used to simulate the case studies described above and same settings in the control experiment of both rainstorms. We selected the triplet nested-grid region of the Mercator map projection (Fig. 5). The spacing of the coarse grid was 27 km and the number of grid points was 150 × 130; the spacing of the medium grid was 9 km and number of grid points was 121 × 121; and the spacing of the fine grid was 3 km

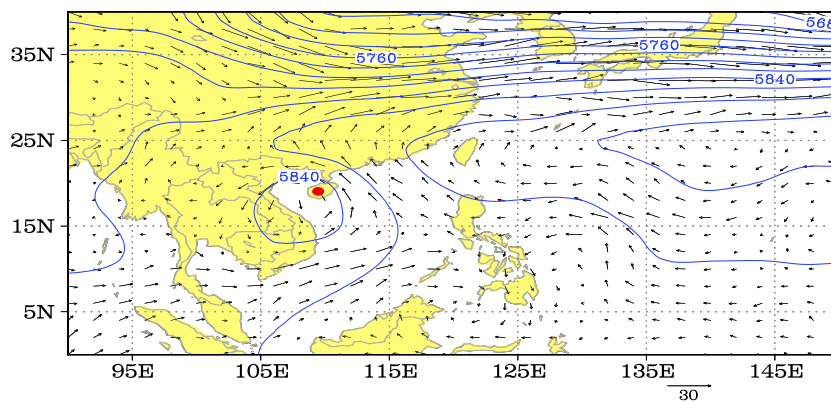


Fig. 3. Wind (black arrow, unit: m/s) and geopotential height (blue line, unit: gpm) at 500 hPa at 1200 UTC 4 Oct 2011. Red filled circle indicates location of Hainan Island.

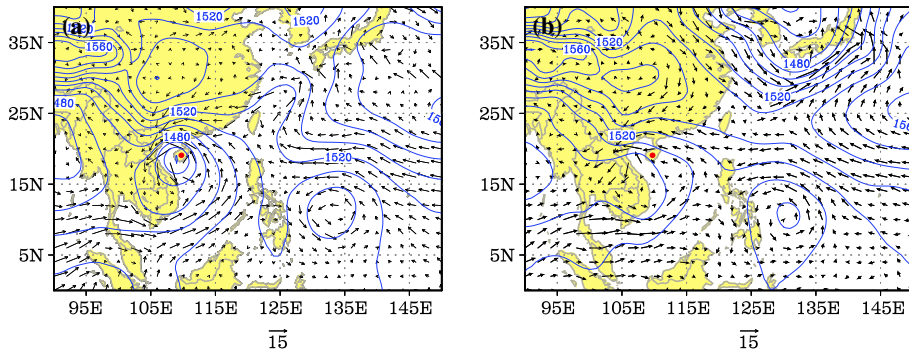


Fig. 4. Wind (black arrow, unit: m/s) and geopotential height (blue line, unit: gpm) at 850 hPa at (a) 1200 UTC 4 Oct; (b) 1200 UTC 5 Oct 2011. Red filled circle indicates location of Hainan Island.

and the number of grid points was 160×154 . We capped the mode at 50 hPa and 37 sigma layers were used in the vertical direction. We used the Yonsei University boundary scheme in the control experiment (Hong et al., 2006) and selected the Noah land-surface model process (Chen and Dudhia, 2001). In addition, the long-wave and short-wave radiation schemes were, respectively, the Rapid Radiative Transfer Model (RRTM) scheme (Mlawer et al., 1997) and the Dudhia scheme (Dudhia, 1989). As our microphysics scheme, we selected the WRF six-class, double-moment (WDM6) scheme (Lim and Hong, 2010). We chose the Grell-Devenyi ensemble scheme (Grell and Dévényi, 2002) for the convective parameterization scheme in D01 and D02, but not for D03. As the first-guess field of the mode, we used the FNL data of the NCEP/NCAR global grid point reanalysis with a horizontal resolution of $1^\circ \times 1^\circ$ and a frequency of four times a day. The integration step was 150 s. We assimilated the radar velocity and reflectivity data with the WRF-3DVAR system at 0000 UTC 5 October 2010 and 1200 UTC 4 October 2011. The simulation periods were from 0000 UTC 5 October to 0000 UTC 6 October 2010 and from 1200 UTC 4 October to 1200 UTC 5 October 2011, which were the two days with the heaviest precipitation in these two continuous rainstorms. The integration time was 24 h in both cases. In case A, the actual observed 24 h accumulated rainfall totaled 881.8 mm, whereas in case B, it was only 333.6 mm.

To examine the impact of latent heat in the various cloud microphysics processes of precipitation with different intensities based on a control experiment of the WDM6 cloud microphysics scheme (CNTL), we conducted three sensitivity experiments characterized by different

latent heat release processes (Table 1). We labeled one of the experiments the NDP experiment, which involved no release of deposition latent heat. In other words, we did not take into consideration the latent heat release of some microphysical processes, such as the growth of snow deposition and cloud ice deposition, the initiation of cloud ice or the growth of graupel deposition. We labeled the second the NFZ experiment, which involved no release of freezing latent heat. Simply speaking, we did not take into account the latent heat release of microphysical processes such as the collection of snow or graupel, the collection of rainwater by cloud ice, graupel, or snow, the homogeneous growth and non-homogeneous growth of cloud ice, or the freezing of rainwater into graupel. We labeled the third the NCEVP experiment, in which we did not take into account the release of latent heat from cloud water evaporation. In contrast to the study by Fernández-González et al. (2016), rather than exclude any microphysical process, we excluded latent heat only.

4. Quantitative verification of CNTL experiment

Ebert (2008) summarized 12 prediction verification methods, two of which we adopted in this study. The first is the fractions skill score (FSS), which we used to compare the observed and predicted precipitation coverages. In addition, based on the distribution of precipitation, we were able to determine if the forecast results were accurate (e.g., Roberts and Lean, 2008; Zacharov and Řezáčová, 2009). The FSS ranges from 0 to 1, whereby the greater the value, the better is the prediction. FSS = 1 indicates that the forecast result is perfect and FSS = 0 indicates a poor forecast result. The other method is the Hanssen skill score (HSS), which we used to evaluate the prediction correctness. HSS ranges from -1 to 1. HSS = 1 indicates that the mode can accurately predict the occurrence of weather processes (e.g., Mullan and Thompson, 2006; Abhilash et al., 2014). HSS = -1 indicates that the number of hits = 0 and the number of correct rejections = 0, or that weather events cannot be correctly predicted at all.

To compare the observed data and mode output results, we used the Cressman interpolation method to interpolate the site data to the mode grid points. We selected the region (108.6010° E– 111.1914° E,

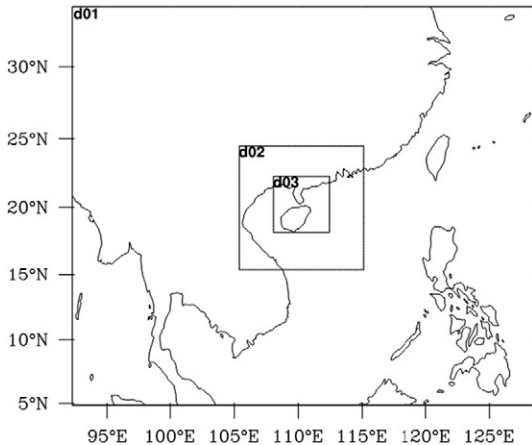


Fig. 5. Three nested domains used for CNTL experiment: D01, D02, and D03.

Table 1
Experiment design for case A and case B.

Experiment	Description
CNTL	WDM6 cloud microphysical scheme
NDP	WDM6, but without latent heat release from deposition
NFZ	WDM6, but without latent heat release from freezing
NCEVP	WDM6, but without latent heat release from cloud water evaporation

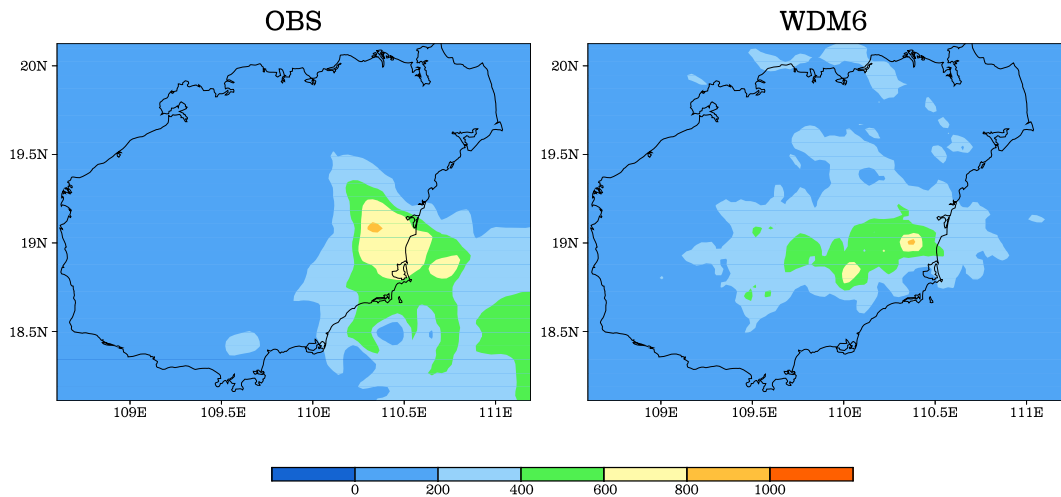


Fig. 6. 24-h accumulated precipitation from the observation and CNTL experiment from 0000 UTC 5 Oct to 0000 UTC 6 Oct 2010 (unit: mm).

18.11069° N–20.12471° N) to grade the results so as to minimize the interpolation error. This region contains 97×80 grid points. Hence, we chose the following sizes of the neighboring area: 1×1 , 3×3 , 5×5 , 9×9 , 17×17 , 33×33 , and 65×65 . FSS = −999.0 suggests that there is no grid point with a precipitation value more than a certain value k in the mode and observation results. If HSS = −999, this indicates that there is no grid point where the predicted precipitation value exceeds k.

4.1. Case A

We interpolated the observed data to the mode grid point with a grid spacing of 3 km. Fig. 6 shows the cumulative precipitation distribution of the observed data and the CNTL experiment. The simulated precipitation center and intensity were consistent with the actual conditions. Because the storm rainfall exceeded 800 mm, we chose the following precipitation threshold values: k = 1, 10, 25, 50, 100, 200, 400, 600, and 800. S = 1 corresponds to traditional point-to-point scoring.

Table 2 shows the FSS scores of the CNTL experiment. In general, the larger is the neighborhood area, the greater is the FSS, and the better are the model simulation results. As the precipitation threshold decreased, FSS grew, and the simulation result improved. The WDM6 experiment successfully simulated the precipitation area (k = 1). For threshold values k of 10, 25, 50, and 100, the FSSs were all above 0.6. When precipitation was above 600 mm, the maximum value of FSS was 0.3. The simulation results for precipitation above 800 mm were general and the maximum FSS value reached 0.52. There was no precipitation above 1000 mm in either the observation

or simulation (Fig. 6). It is reasonable to state that the maximum precipitation for both the observation and simulation was between 800 and 1000 mm.

Table 3 lists the HSS values in the CNTL experiment. When k = 1 and s = 65, the predictions were very accurate. When k = 1 and more than 800 mm of precipitation was predicted to occur in regions with sizes greater than 9×9 grid points, the forecast were relatively accurate. For regions greater than or equal to 5×5 with precipitation over 800 mm, the predictions were relatively accurate, and the maximum HSS value could reach 0.89. When k = 10, 25, 50, 100, 200, 400, and 600, the HSS values were also positive.

4.2. Case B

Fig. 7 shows that the simulated precipitation center and intensity were consistent with the actual conditions. In this case, the maximum precipitation was less than 400 mm, so we selected the following precipitation threshold values: k = 1, 10, 25, 50, 100, 200, and 300. Table 4 shows the FSS score of the CNTL experiment, in which no precipitation of more than 400 mm occurred in the experimental and observation grid points (Fig. 7). The precipitation areas (k = 1) mostly matched. When k equaled 10, 25, 50, 100, and 200, the forecast results were also excellent and the FSS was above 0.5. For precipitation above 300 mm, the maximum value of FSS reached 0.49 and the minimum was 0.16.

We can see in Table 5 that when k = 10, 25, 50, 100, and 200, the HSS values are all positive, indicating that the forecast results of the CNTL experiment were good. When more than 300 mm precipitation was predicted to occur and the region size was 17×17 grid points or more, the forecast results were all relatively accurate and the maximum

Table 2
FSS scores of CNTL for case A.

Grid points	Precipitation threshold (mm)								
	1	10	25	50	100	200	400	600	800
65 × 65	1.00	1.00	1.00	1.00	0.98	0.95	0.80	0.30	0.52
33 × 33	1.00	1.00	1.00	0.99	0.92	0.71	0.63	0.26	0.48
17 × 17	1.00	1.00	0.99	0.95	0.82	0.54	0.41	0.20	0.43
9 × 9	1.00	1.00	0.97	0.90	0.73	0.46	0.31	0.20	0.34
5 × 5	1.00	1.00	0.96	0.87	0.68	0.41	0.25	0.19	0.18
3 × 3	1.00	0.99	0.95	0.85	0.65	0.39	0.22	0.17	0.00
1 × 1	1.00	0.99	0.93	0.83	0.61	0.35	0.19	0.14	0.00

Table 3
HSS scores of CNTL for case A.

Grid points	Precipitation threshold (mm)								
	1	10	25	50	100	200	400	600	800
65 × 65	1.00	0.53	0.53	0.38	0.08	0.21	0.38	0.78	0.89
33 × 33	−0.00	0.52	0.49	0.24	0.15	0.19	0.41	0.66	0.71
17 × 17	−0.00	0.49	0.43	0.09	0.18	0.26	0.26	0.30	0.57
9 × 9	−0.00	0.29	0.24	0.20	0.18	0.20	0.17	0.20	0.38
5 × 5	−0.00	0.53	0.32	0.19	0.16	0.17	0.14	0.14	0.18
3 × 3	−0.00	0.52	0.30	0.17	0.16	0.16	0.12	0.11	−0.00
1 × 1	−0.00	0.51	0.26	0.15	0.16	0.16	0.10	0.08	−0.00

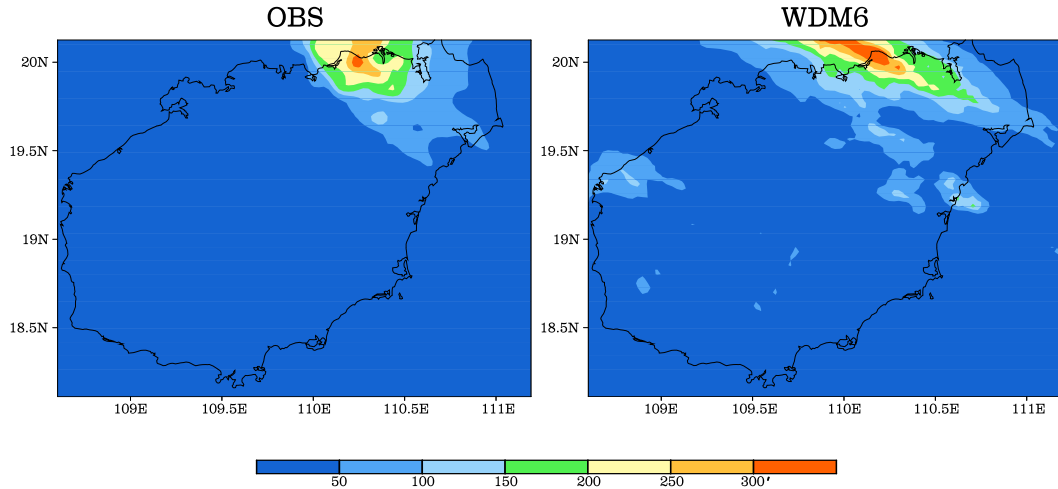


Fig. 7. 24-h accumulated precipitation from the observation and CNTL experiment from 1200 UTC 4 Oct to 1200 UTC 5 Oct 2011(unit: mm).

HSS value was 0.58. Predictions for the occurrence of precipitation over 300 mm were rather accurate. The maximum HSS value was 0.95 and the minimum value was 0.5.

The scores of these two methods were higher than typical values and long-term averages in many places (e.g., McBride and Ebert, 2000; Accadia et al., 2003; Jie and Wu, 2010; Zacharov et al., 2013). Based on the scores of these two methods, we can conclude that the CNTL experiment reasonably reproduced the two torrential rain processes in Hainan.

5. Comparison of sensitivity experiments

5.1. Precipitation

Based on case A (Fig. 8) and compared with the CNTL experiment, the NDP experiment showed the least precipitation with a maximum precipitation less than 500 mm. In addition, the coverage area that experienced more than 100 mm precipitation was the smallest due to the absence of the heating effect of deposition. The rainfall belt of the NFZ experiment was basically the same as that of the CNTL experiment, but the precipitation intensity was weaker compared to the CNTL experiment. Its maximum precipitation was more than 600 mm, because there was no release of latent heat. Rainfall in the NCEP experiment was also reduced with the precipitation center in the north. Having been affected by the cooling effect of evaporation of the middle- and lower-altitude cloud water, the maximum precipitation was less than 600 mm. The hourly precipitation in the NDP experiment was always the lowest of the three (Fig. 9). Moreover, its evolving trend was

inconsistent with the CNTL, while the evolving trend of precipitation in the NFZ experiment generally coincided with that of the CNTL experiment. Its precipitation intensity, however, was weaker. Precipitation in the NCEVP experiment was not less than that in the CNTL experiment until 14:00, and then became weaker afterwards.

With respect to case B (Fig. 10), the simulated accumulative precipitation in the NDP experiment also was lowest due to the absence of the heating effect of deposition. The maximum precipitation was more than 200 mm and less than 300 mm, and the simulated rainfall belt in the NFZ experiment was similar to that in the CNTL experiment. Furthermore, its maximum precipitation level was also close to that of the CNTL experiment. Without the freezing latent heat release, the maximum precipitation in the Haikou area was slightly weaker than that in the CNTL experiment, and the rain belt simulated in the NCEVP experiment moved northward. Because there was no cooling effect generated by cloud water evaporation, its precipitation was higher, with a maximum rainfall of more than 500 mm and a significant intensification of heavy rain. Fig. 11 shows no significant difference in the precipitation of the NFZ and CNTL experiments. The evolution of the precipitation frequency in the NDP was consistent with that of the CNTL, but its precipitation intensification and extinction were more obvious than those of the CNTL, except for the hour from 20:00 to 21:00, when the precipitation in the NCEVP experiment was higher than in the CNTL. The rainfall of the CNTL weakened after 08:00 on October 5, whereas the precipitation of the NCEP was strengthened.

5.2. Vertical velocity field

At about 2:00 on October 5, the vertical velocity of the four case A experiments reached the maximum value (Fig. 12). The lowest velocity

Table 4
FSS scores of CNTL for case B.

Grid points	Precipitation threshold (mm)						
	1	10	25	50	100	200	300
65 × 65	0.99	0.76	0.77	0.84	0.89	1.00	0.49
33 × 33	0.98	0.69	0.74	0.85	0.90	0.98	0.48
17 × 17	0.97	0.72	0.73	0.83	0.90	0.96	0.47
9 × 9	0.95	0.71	0.68	0.72	0.85	0.93	0.45
5 × 5	0.93	0.70	0.65	0.64	0.80	0.88	0.36
3 × 3	0.91	0.68	0.62	0.59	0.75	0.80	0.26
1 × 1	0.89	0.64	0.57	0.52	0.66	0.67	0.16

Table 5
HSS scores of CNTL for case B.

Grid points	Precipitation threshold (mm)						
	1	10	25	50	100	200	300
65 × 65	0.02	0.06	0.05	0.06	0.42	0.90	0.95
33 × 33	0.03	0.06	0.09	0.20	0.68	0.93	0.97
17 × 17	0.12	0.23	0.30	0.55	0.79	0.92	0.96
9 × 9	0.18	0.30	0.48	0.68	0.86	0.91	0.94
5 × 5	0.24	0.38	0.53	0.69	0.84	0.79	0.85
3 × 3	0.27	0.43	0.54	0.66	0.83	0.72	0.73
1 × 1	0.31	0.48	0.55	0.63	0.82	0.67	0.50

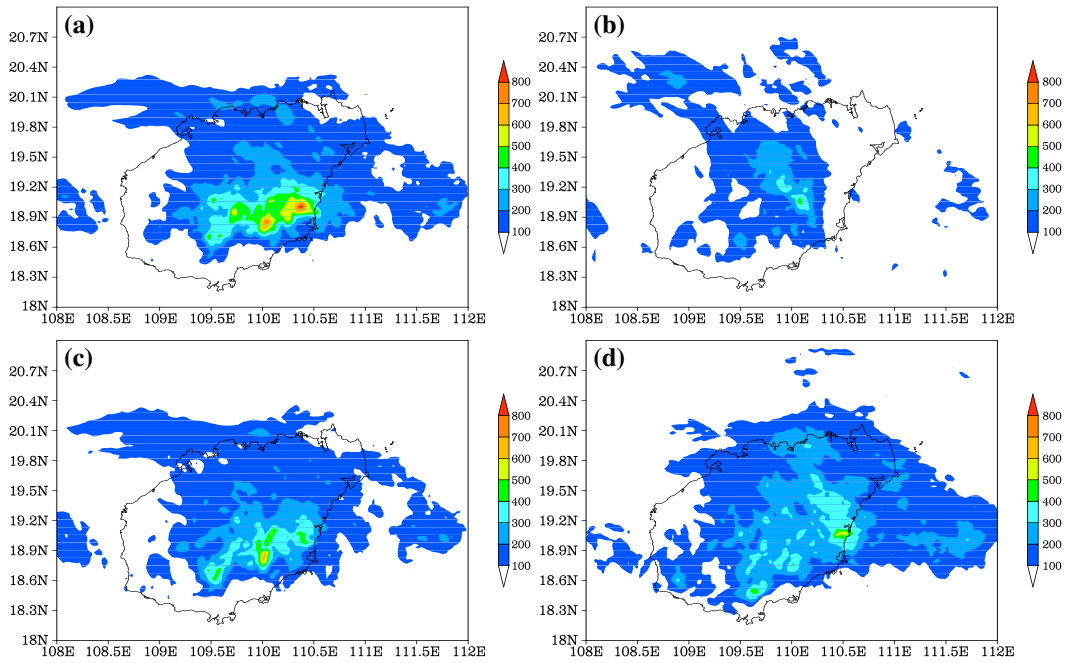


Fig. 8. 24-h accumulated precipitation from 0000 UTC 5 Oct to 0000 UTC 6 Oct 2010 (unit: mm). (a) CNTL; (b) NDP; (c) NFZ; (d) NCEVP.

was in the NDP experiments and the range of the vertical rise zone decreased. The strongest areas were located near the 350-hPa level, and the ascending motion was so weak in the high-altitude level that sinking movement could occur, because there was no deposition latent heating in the middle- and high-altitude levels, which reduced their temperature difference at higher altitude. In this case, the instability of the stratification decreased and the ascending motion weakened. In the NCEVP experiment, the vertical movement was the strongest and the evolution trend of the vertical velocity was consistent with that of precipitation. The ascending motion was stronger than in the control experiment before 14:00, and then the vertical motion was weaker than in the CNTL experiment. The reason for this is that there was no evaporative cooling effect of cloud water in the middle and lower troposphere, leading to an increased temperature difference at upper troposphere. Thus, vertical movement at upper troposphere was enhanced. Moreover, the ascending motion would have affected the microphysical processes of the cloud, thus strengthening the

heating effect of deposition at upper troposphere, reducing the temperature gradient of the vertical field, and ultimately weakening the vertical motion.

Fig. 13 shows that all four case-B experiments reflect the rising motion in the middle and lower troposphere at 15:00. As there was no heating effect of deposition in the NDP experiment, the movements at upper troposphere were mainly descending. In the NFZ experiment, due to the absence of the heating effect caused by freezing in the middle altitude, the descending movement at upper troposphere strengthened while the ascending motion weakened. The vertical velocity in the NCEVP experiment corresponded to the hourly precipitation evolution in Fig. 11. This shows that its ascending movements within 24 h were all stronger than in the CNTL experiment. The reason for this might be that cloud water was more abundant at lower troposphere in case B. Without the evaporative cooling effect of cloud water, the temperature gradient between the middle and lower troposphere increased, and the vertical ascending movement strengthened, thus enhancing the cooling effect of condensation. In this case, the temperature gradient at upper troposphere increased, which was conducive to strengthening the vertical movement.

5.3. Vertical distribution of hydrometeors

The distribution characteristics of the average mixing ratio of hydrometeors differed in the precipitation areas of the different experiments. In case A (Fig. 14), unlike the CNTL experiment; there was no latent heat release of deposition in the NDP experiment. The vertical movement weakened and the vertical distribution coverage and the cloud ice, snow, and graupel contents all decreased. Moreover, the rainwater content reduced as well. The cloud water in middle altitudes decreased whereas it increased in lower troposphere. In the NFZ experiment, the mixing ratio of cloud and ice was similar to that in the CNTL experiment. The distribution coverage of cloud ice was slightly smaller than that of the CNTL experiment. The differences in distributions and in the rainwater, snow, and cloud water contents in the two experiments were very small. In addition, the distribution coverage and graupel content were also smaller than those in the CNTL. In the initial 14 h of the NCEVP

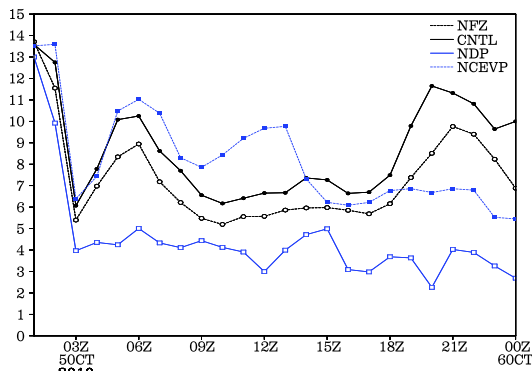


Fig. 9. Hourly precipitation (unit: mm) from 0100 UTC 5 Oct to 0000 UTC 6 Oct 2010 in the rainfall region (109°E–111°E, 18.5°N–19.5°N).

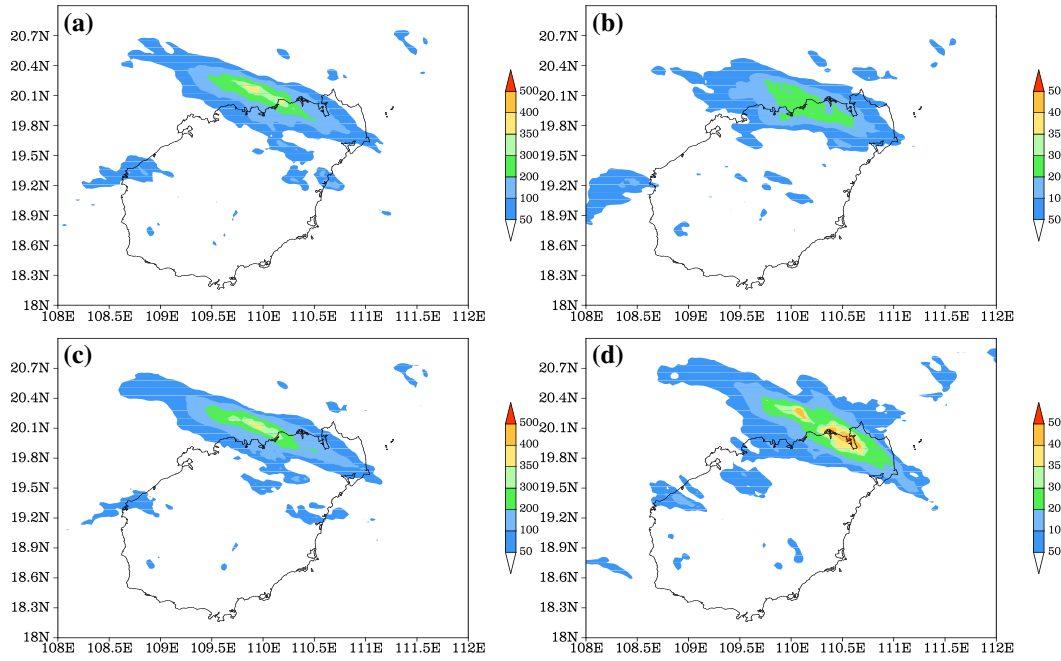


Fig. 10. 24-h accumulated precipitation from 1200 UTC 4 Oct to 1200 UTC 5 Oct 2011 (unit: mm). (a) CNTL; (b) NDP; (c) NFZ; (d) NCEVP.

experiment, there was more snow, graupel, cloud ice, and rainwater content than in the CNTL experiment. Afterwards, they became less than in the CNTL. There was no significant content difference between the two experiments.

In case B (Fig. 15), since there was no heating effect of deposition in the NDP experiment, the cloud development was weakened in the vertical direction. In addition, the cloud ice and snow contents increased with a reduced distribution in height. The graupel content increased as well. However, there was no significant difference in the distribution location. Moreover, the rainwater content showed no significant changes, but the cloud water increased because of the weakened ascending movement at upper troposphere and the enhanced vertical movement in middle and lower troposphere. Without the heating effect of freezing, the cloud ice, snow, and graupel contents dropped in the NFZ experiment. Although there were no significant changes in cloud water or rainwater; with the absence of the evaporative cooling effect of cloud water, the distribution coverage and range of cloud ice, snow, and

graupel expanded in the vertical direction in the NCEVP experiment. The rainwater increased as well, but there was no significant change in cloud water.

5.4. Heating profile of latent heat

Next, we calculated the average latent heat in the precipitation area to obtain a time–height profile. In case A (Fig. 16), the height and intensity of the heating effect of latent heat in the NDP experiment were smaller than those in the control experiment, and the maximum heating rate after 3:00 was 0.15 K/h. Without the heating effect of freezing, the height and strength of the heating effect of latent heating were slightly reduced, yet the reduction was not as significant as that in the NDP experiment. After 3:00, the maximum heating rate was 2 K/h. Since there was no evaporative cooling effect of cloud water, compared with the CNTL experiment, the heating rate of latent heat in the NCEVP experiment was larger in the initial stage and then decreased. After 3:00, the maximum heating rate was above 0.25 K/h.

In case B, Fig. 17 shows that due to the absence of the heating effect of deposition at upper troposphere in the NDP experiment, the heating effect of latent heat in the middle altitude was greater compared to that in the control experiment but was smaller at upper troposphere, with a maximum value of 0.15 K/h. There was no significant difference in the heating rate of latent heat in the NFZ and CNTL experiments. In the NCEVP experiment, the absence of the evaporative cooling effect of cloud water increased the convective instability. In addition, compared to the CNTL experiment, the height and intensity of the heating effect of latent heat in the NCEVP experiment were larger.

6. Summary

Using the WRF and WRF-3DVAR models, we performed a series of simulations of two autumn rainstorms in Hainan Island. The results of neighborhood-method FSS and HSS scoring indicate that the WRF mode of the WDM6 microphysical scheme reasonably reproduced the two rainstorm processes of different intensities. Based on the success

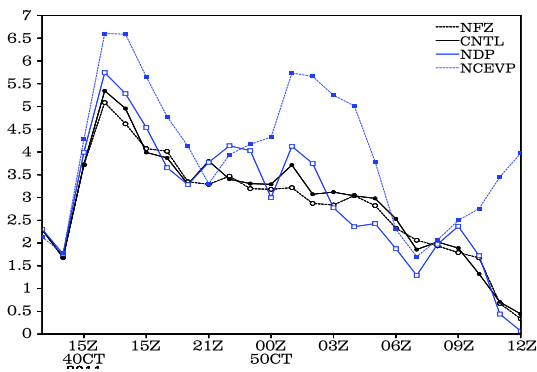


Fig. 11. Hourly precipitation (unit: mm) from 1300 UTC 4 Oct to 1200 UTC 5 Oct 2011 in the rainfall region (109°E–111°E, 19.7°N–20.7°N).

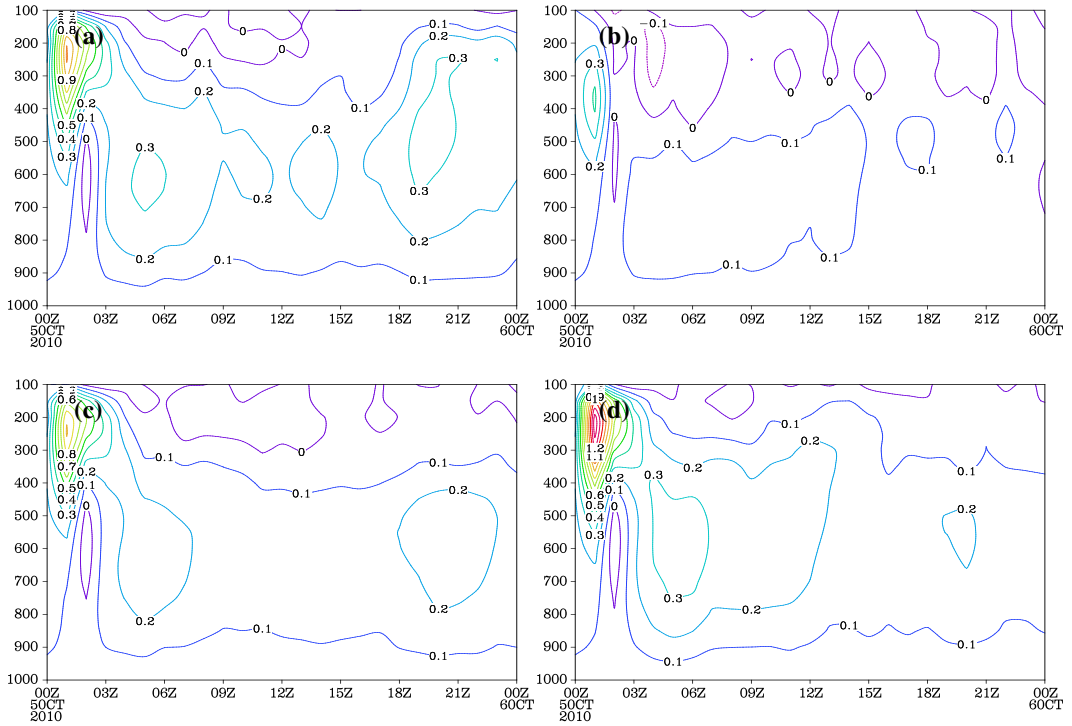


Fig. 12. Regional averaged (109°E - 111°E , 18.5°N - 19.5°N) vertical velocity from different simulations for case A (unit: m/s). (a) CNTL; (b) NDP; (c) NFZ; (d) NCEVP.

of the control experiment, we conducted three sensitivity experiments. In these experiments, we examined the effects of latent heat in various microphysical processes on precipitation with different intensities.

First, the effects of latent heat release on precipitation were different. When there was no latent heat of deposition, the precipitation was reduced. Moreover, as precipitation increased, the heating effect of condensation became more significant. The latent heat of freezing exerted

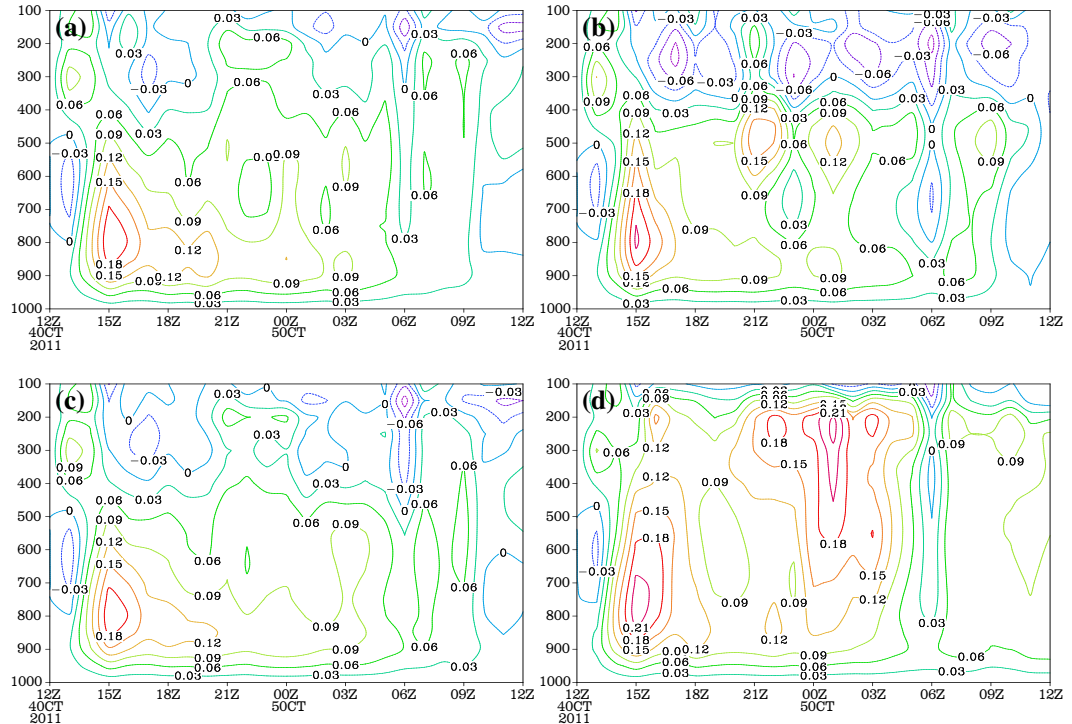


Fig. 13. Regional averaged (109°E - 111°E , 19.7°N - 20.7°N) vertical velocity from different simulations for case B (unit: m/s). (a) CNTL; (b) NDP; (c) NFZ; (d) NCEVP.

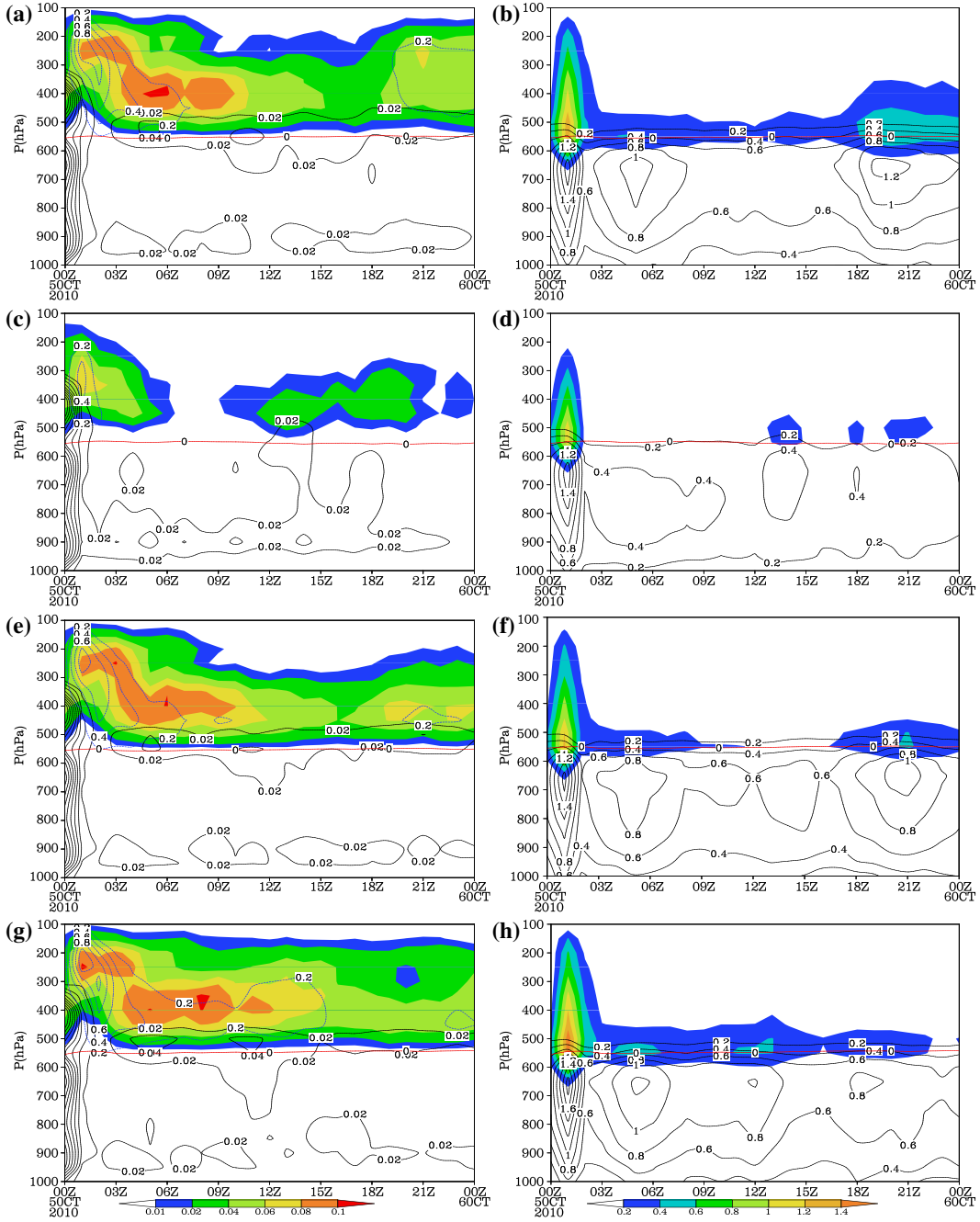


Fig. 14. Mixing ratios (unit: g/kg) of different moisture variables from 0000 UTC 5 Oct to 0000 UTC 6 Oct 2010 in the rainfall region (109°E - 111°E , 18.5°N - 19.5°N). In (a), (c), (e), and (g), there are cloud water (black solid line), cloud ice (shaded), and snow (blue dotted line). In (b), (d), (f), and (h), there are rain water (black solid line) and graupel (shaded). (a), (b) CNTL; (c), (d) NDP; (e), (f) NFZ; (g), (h) NCEVP.

the least impact on precipitation. The greater was the precipitation, the more significant was the heating effect of freezing. The influence of the evaporative cooling effect of cloud water on different precipitation systems differed and was inversely proportional to the precipitation. Without the evaporative cooling effect, the precipitation that was initially large decreased, and in contrast, small levels of precipitation increased. However, in the initial stage of rainfall, all precipitation was enhanced.

Secondly, in the absence of the heating effect of deposition at upper troposphere or the heating effect of freezing in middle altitudes, the ascending movement at upper troposphere weakened or the descending movement strengthened. Without the evaporative cooling effect of

cloud water, for cases with low precipitation in 2011, the strong ascending zone enhanced in the middle and lower troposphere. The mutual effect of vertical movement and cloud microphysical processes led to an increase in the overall vertical ascending velocity. For individual heavy-precipitation cases in 2011, strong convective regions at upper troposphere were also strengthened. With their mutual interaction with cloud microphysical processes, vertical movements were weakened.

Thirdly, the vertical distribution and content of hydrometeors were affected in the absence of the heating effect of deposition. Under conditions with heavy precipitation, the contents of cloud ice, snow, graupel, and rainwater all reduced. However, for lower levels of precipitation,

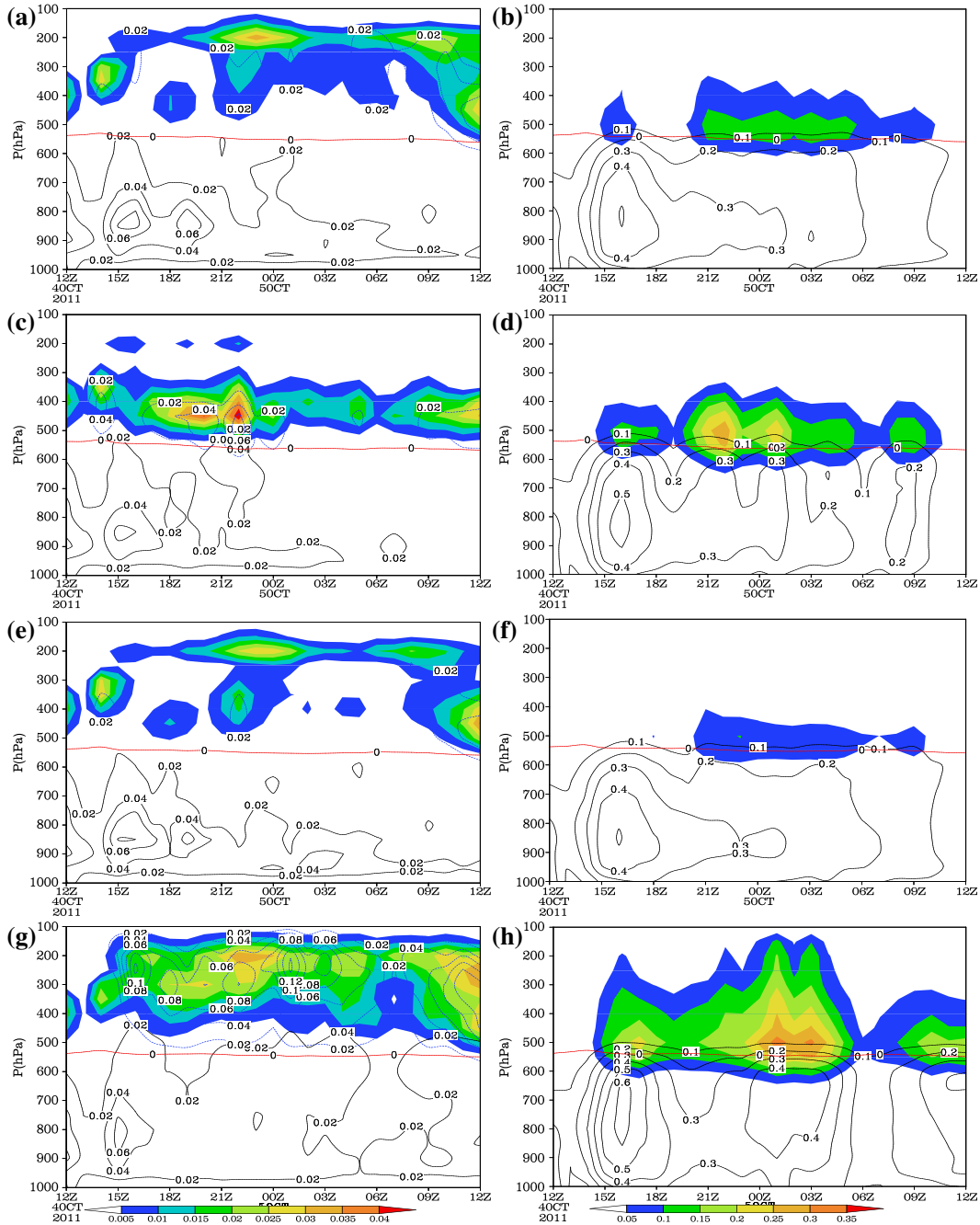


Fig. 15. Mixing ratios (unit: g/kg) of different moisture variables from 1200 UTC 4 Oct to 1200 UTC 5 Oct 2011 in the rainfall region (109°E - 111°E , 19.7°N - 20.7°N). In (a), (c), (e), and (g), there are cloud water (black solid line), cloud ice (shaded), and snow (blue dotted line). In (b), (d), (f), and (h), there are rainwater (black solid line) and graupel (shaded). (a), (b) CNTL; (c), (d) NDP; (e), (f) NFZ; (g), (h) NCEVP.

the rainwater content increased whereas the contents of cloud ice and snow dropped at upper troposphere. At middle troposphere, the contents of cloud ice, snow, and graupel increased. This phenomenon was mainly caused by the various strong convective areas of the different precipitation systems as well as the impact on convection by the heating effect of condensation. The heating effect of freezing had little impact on the vertical distribution or content of hydrometeors. Without this impact, the graupel content slightly decreased. In the absence of the evaporative cooling effect of cloud water, the snow, graupel, cloud ice, and rainwater contents all increased in the preliminary rainfall stage. Afterwards, the vertical movement and cloud microphysics interacted and

affected each other. In the 2010 cases, the contents of snow, graupel, cloud ice, and rainwater decreased in the latter period. The 2011 cases exhibited the opposite situation.

Fourthly, in the absence of the heating effect of deposition, the heating effect of latent heat in heavy precipitation decreased while in relatively weak precipitation, the heating effect of latent heat at middle and lower troposphere increased but reduced at upper troposphere. The heating effect of freezing exerted little impact on the heating effect of latent heat in precipitation. In the absence of any evaporative cooling effect of cloud water, the heating effect of latent heat in strong precipitation first increased and then dropped, whereas in relatively weak

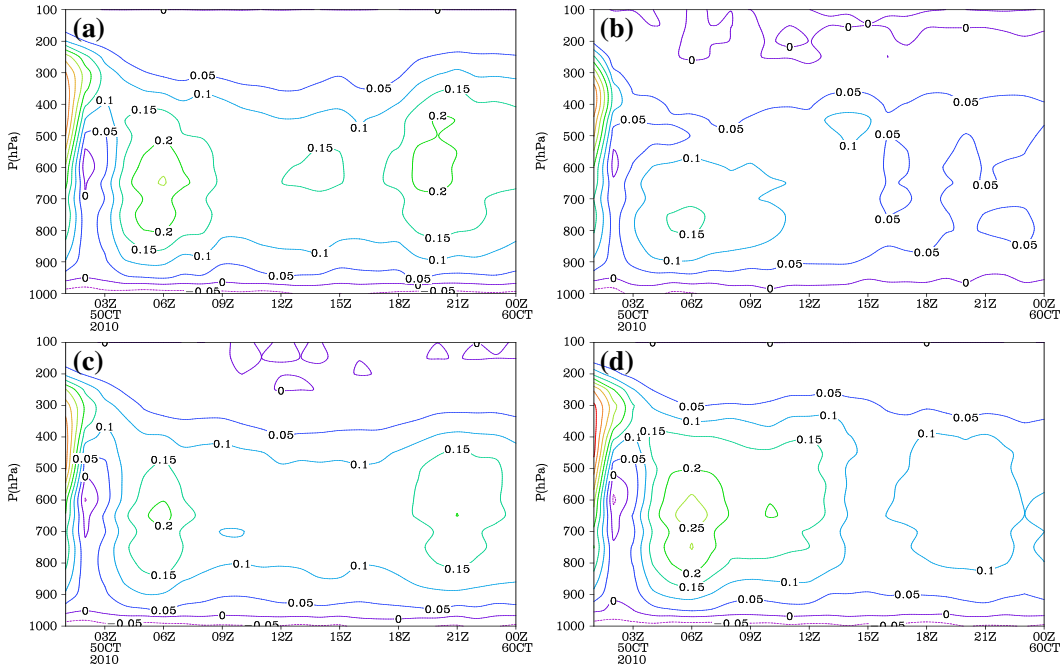


Fig. 16. Regional averaged (109°E - 111°E , 18.5°N - 19.5°N) latent heating rate from different simulations for case A (unit: K/h). (a) CNTL; (b) NDP; (c) NFZ; (d) NCEVP.

precipitation, it simply increased. This phenomenon was caused by the different influences of the evaporative cooling effect on the vertical movements of different precipitation systems.

These simulation results show that microphysical latent heat processes have different effects on precipitation of different intensities or at different stages. At upper troposphere, latent heat is released and the atmosphere gradually becomes stable, thus inhibiting the development of convection. At lower troposphere, it is absorbed, which causes instability and conditions become conducive to convection. Our results also indicate microphysical process to be very important for the occurrence, development, and alteration in precipitation intensity. However,

it wasn't the only determinant. In the precipitation process, there are complex relationships between microphysical processes and other dynamic or thermal processes. The impact of interactions between these processes on the occurrence of precipitation requires further study.

Funding

This work was supported by the National Natural Science Foundation of China (Grant No. 41275060); the National Key Basic Research Program

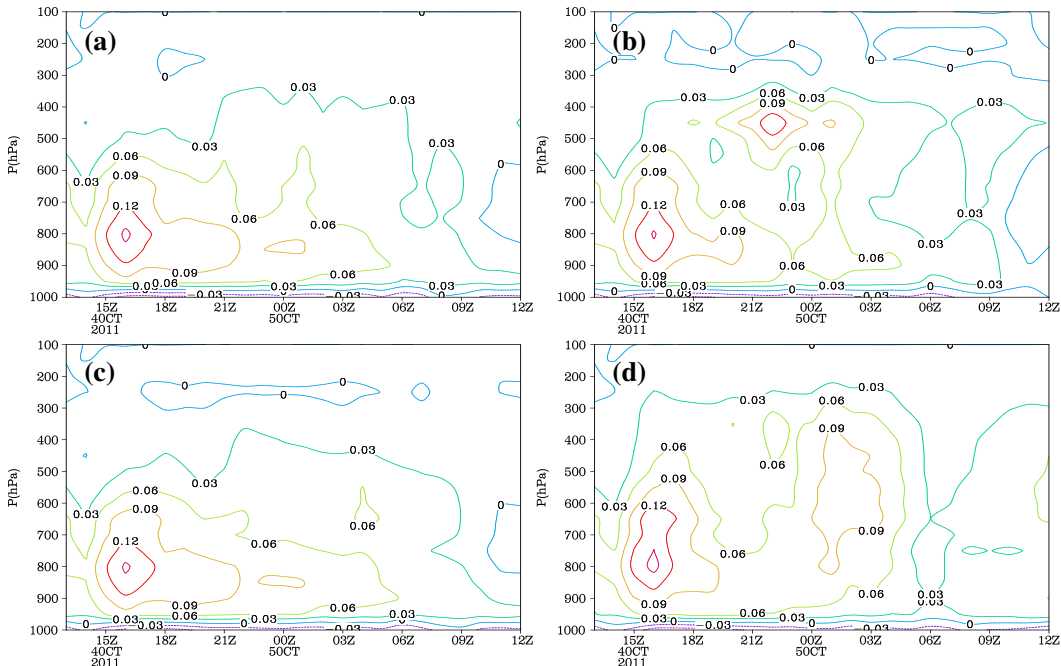


Fig. 17. Regional averaged (109°E - 111°E , 19.7°N - 20.7°N) latent heating rate from different simulations for case B (unit: K/h). (a) CNTL; (b) NDP; (c) NFZ; (d) NCEVP.

of China (Grant No. 2014CB953903); and the National Key Research and Development Program of China (Grant No. 2016YFA0602701).

References

- Abhilash, S., Sahai, A.K., Borah, N., Chattopadhyay, R., Joseph, S., Sharmila, S., De, S., Goswami, B.N., Kumar, A., 2014. Prediction and monitoring of monsoon intraseasonal oscillations over Indian monsoon region in an ensemble prediction system using CFSv2. *Clim. Dyn.* 42:2801–2815. <http://dx.doi.org/10.1007/s00382-013-2045-9>.
- Accadia, C., Mariani, S., Casaioli, M., Lavagnini, A., Speranza, A., 2003. Sensitivity of precipitation forecast skill scores to bilinear interpolation and a simple nearest-neighbor average method on high-resolution verification grids. *Weather Forecast.* 18:918–932. [http://dx.doi.org/10.1175/1520-0434\(2003\)018-0918:SOPFSS>2.0.CO;2](http://dx.doi.org/10.1175/1520-0434(2003)018-0918:SOPFSS>2.0.CO;2).
- Adams-Selin, R.D., van den Heever, S.C., Johnson, R.H., 2013. Sensitivity of bow echo simulation to microphysical parameterizations. *Weather Forecast.* 28:1188–1209. <http://dx.doi.org/10.1175/WAF-D-12-00108.1>.
- Barthe, C., Hoarau, T., Bovalo, C., 2016. Cloud electrification and lightning activity in a tropical cyclone-like vortex. *Atmos. Res.* 180:297–309. <http://dx.doi.org/10.1016/j.atmosres.2016.05.023>.
- Chen, F., Dudhia, J., 2001. Coupling an advanced land-surface/hydrology model with the Penn State/NCAR MM5 modeling system: part I. Model description and implementation. *Mon. Weather Rev.* 129:569–585. [http://dx.doi.org/10.1175/1520-0493\(2001\)129<0569:CALSH>2.0.CO;2](http://dx.doi.org/10.1175/1520-0493(2001)129<0569:CALSH>2.0.CO;2).
- Colle, B.A., Garvert, M.F., Wolfe, J.B., Mass, C.F., Woods, C.P., 2005. The 13–14 December 2001 IMPROVE-2 event. Part III: simulated microphysical budgets and sensitivity studies. *J. Atmos. Sci.* 62:3535–3558. <http://dx.doi.org/10.1175/JAS3521>.
- Dudhia, J., 1989. Numerical study of convection observed during the winter monsoon experiment using a mesoscale two-dimensional model. *J. Atmos. Soc.* 46:3077–3107. [http://dx.doi.org/10.1175/1520-0469\(1989\)046<3077:NSCOD>2.0.CO;2](http://dx.doi.org/10.1175/1520-0469(1989)046<3077:NSCOD>2.0.CO;2).
- Dudhia, J., Hong, S.Y., Lim, K.S., 2008. A new method for representing mixed-phase particle fall speeds in bulk microphysics parameterizations. *J. Meteor. Soc. Japan* 86A: 33–44. <http://dx.doi.org/10.2151/jmsj.86A.33>.
- Ebert, E.E., 2008. Fuzzy verification of high-resolution gridded forecasts: a review and proposed framework. *Meteorol. Appl.* 15:51–64. <http://dx.doi.org/10.1002/met.25>.
- Fernández-González, S., Wang, P.K., Gascón, E., Valero, F., Sánchez, J.L., 2016. Latent cooling and microphysics effects in deep convection. *Atmos. Res.* 180:189–199. <http://dx.doi.org/10.1016/j.atmosres.2016.05.022>.
- Flossmann, A.J., Wobrock, W., 2010. A review of our understanding of the aerosol–cloud interaction from the perspective of a bin resolved cloud scale modelling. *Atmos. Res.* 97:478–497. <http://dx.doi.org/10.1016/j.atmosres.2010.05.008>.
- Gao, S.T., Ping, F., Li, X.F., 2006. Cloud microphysical processes associated with the diurnal variations of tropical convection: a 2D cloud resolving modelling study. *Meteorol. Atmos. Phys.* 91:9–16. <http://dx.doi.org/10.1007/s00703-005-0108-5>.
- Grell, G.A., Dévényi, D.A., 2002. A generalized approach to parameterizing convection combining ensemble and data assimilation techniques. *Geophys. Res. Lett.* 29 (14): 1693. <http://dx.doi.org/10.1029/2002GL015311>.
- Guo, C.-W., Xiao, H., Yang, H.-L., Tang, Q., 2015. Observation and modeling analyses of the macro- and microphysical characteristics of a heavy rain storm in Beijing. *Atmos. Res.* 156:125–141. <http://dx.doi.org/10.1016/j.atmosres.2015.01.007>.
- Hong, S.-Y., Noh, Y., Dudhia, J., 2006. A new vertical diffusion package with an explicit treatment of entrainment processes. *Mon. Weather Rev.* 134:2318–2341. <http://dx.doi.org/10.1175/MWR3199.1>.
- Huang, Y.-C., Wang, P.K., 2017. The hydrometeor partitioning and microphysical processes over the Pacific warm pool in numerical modeling. *Atmos. Res.* 183:308–321. <http://dx.doi.org/10.1016/j.atmosres.2016.09.009>.
- Jankov, I., Gallus Jr., W.A., Segal, M., Shaw, B., Koch, S.E., 2005. The impact of different WRF model physical parameterizations and their interactions on warm season MCS rainfall. *Weather Forecast.* 6:1048–1060. <http://dx.doi.org/10.1175/WAF888.1>.
- Jankov, I., Gallus Jr., W.A., Segal, M., Shaw, B., Koch, S.E., 2007. Influence of initial conditions on the WRF–ARW model QPF response to physical parameterization changes. *Weather Forecast.* 22:501–519. <http://dx.doi.org/10.1175/WAF998.1>.
- Jiang, B.L., Huang, B., Lin, W.S., Xu, S.S., 2016. Investigation of the effects of anthropogenic pollution on typhoon precipitation and microphysical processes using WRF-Chem. *J. Atmos. Sci.* 73 (4):1593–1610. <http://dx.doi.org/10.1175/JAS-D-15-0202.1>.
- Jie, Weihua, Wu, Tongwen, 2010. Hindcast for the 1998 summer heavy precipitation in the Yangtze and Huaihe River valley using BCC_AGCM2.0.1 model. *Chinese J. Atmos. Sci.* 34 (5):962–978 (in Chinese). 10.3878/j.issn.1006-9895.2010.05.11.
- Levin, Z., Gershon, H., Ganor, E., 2005. Vertical distribution of physical and chemical properties of haze particles in the Dead Sea valley. *Atmos. Environ.* 39:4937–4945. <http://dx.doi.org/10.1016/j.atmosenv.2005.04.039>.
- Li, X., Pu, Z.X., 2008. Sensitivity of numerical simulation of early rapid intensification of hurricane Emily (2005) to cloud microphysical and planetary boundary layer parameterizations. *Mon. Weather Rev.* 136:4819–4838. <http://dx.doi.org/10.1175/2008MWR2366.1>.
- Li, X., Shen, X., 2013. Rain microphysical budget in the tropical deep convective regime: a 2-D cloud-resolving modeling study. *J. Meteorol. Soc. Jpn.* 91 (6):801–815. <http://dx.doi.org/10.2151/jmsj.2013-606>.
- Li, J.N., Wang, G., Lin, W.S., He, Q.H., Feng, Y.R., Mao, J.Y., 2013a. Cloud-scale simulation study of typhoon Hagupit (2008) part I: microphysical processes of the inner core and three-dimensional structure of the latent heat budget. *Atmos. Res.* 120: 170–180. <http://dx.doi.org/10.1016/j.atmosres.2012.08.015>.
- Li, J.N., Wang, G., Lin, W.S., He, Q.H., Feng, Y.R., Mao, J.Y., 2013b. Cloud-scale simulation study of typhoon Hagupit (2008) part II: impact of cloud microphysical latent heat processes on typhoon intensity. *Atmos. Res.* 120:202–215. <http://dx.doi.org/10.1016/j.atmosres.2012.08.018>.
- Lim, K.S.S., Hong, S.Y., 2010. Development of an effective double-moment cloud micro-physics scheme with prognostic cloud condensation nuclei (CCN) for weather and climate models. *Mon. Weather Rev.* 138 (138):1587–1612. <http://dx.doi.org/10.1175/2009MWR2968.1>.
- Lin, W.S., Xu, S.S., Sui, C.-H., 2011. A numerical simulation of the effect of the number concentration of cloud droplets on typhoon Chanchu. *Meteorog. Atmos. Phys.* 113: 99–108. <http://dx.doi.org/10.1007/s00703-011-0152-x>.
- McBride, J.L., Ebert, E.E., 2000. Verification of quantitative precipitation forecasts from operational numerical weather prediction models over Australia. *Weather Forecast.* 15:103–121. [http://dx.doi.org/10.1175/1520-0434\(2000\)015_0103:VQOFPFF.2.0.CO;2](http://dx.doi.org/10.1175/1520-0434(2000)015_0103:VQOFPFF.2.0.CO;2).
- McFarquhar, G.M., Zhang, H., Heymsfield, G., Halverson, J.B., Hood, R., Dudhia, J., Marks, F., 2006. Factors affecting the evolution of Hurricane Erin (2001) and the distributions of hydrometeors: role of microphysical processes. *J. Atmos. Sci.* 63:127–150. <http://dx.doi.org/10.1175/JAS3590.1>.
- Mlawer, E.J., Taubman, S.J., Brown, P.D., Iacono, M.J., Clough, S.A., 1997. Radiative transfer for inhomogeneous atmosphere: RTTM, a validated correlated-k model for the long-wave. *J. Geophys. Res.* 102:16663–16682. <http://dx.doi.org/10.1029/97JD00237>.
- Morrison, H., Milbrandt, J.A., 2015. Parameterization of cloud microphysics based on the prediction of bulk ice particle properties. Part I: scheme description and idealized tests. *J. Atmos. Sci.* 72:287–311. <http://dx.doi.org/10.1175/JAS-D-14-0204.1>.
- Mullan, A.B., Thompson, C.S., 2006. Analogue forecasting of New Zealand climate anomalies. *Int. J. Climatol.* 26 (4):485–504. <http://dx.doi.org/10.1002/joc.1261>.
- Pattnaik, S., Krishnamurti, T.N., 2007. Impact of cloud microphysical processes on hurricane intensity. Part II:sensitivity experiments. *Meteorog. Atmos. Phys.* 97:647–662. <http://dx.doi.org/10.1007/s00703-006-0247-y>.
- Roberts, N., Lean, H., 2008. Scale-selective verification of rainfall accumulations from high-resolution forecasts of convective events. *Mon. Weather Rev.* 136:78–97. <http://dx.doi.org/10.1175/2007MWR2123.1>.
- Rogers, R., Black, M., Chen, S.S., Black, R., 2007. An evaluating microphysical fields from mesoscale model simulations of tropical cyclones. Part I: comparisons with observations. *J. Atmos. Sci.* 64:1811–1834. <http://dx.doi.org/10.1175/JAS3932.1>.
- Rosenfeld, D., Woodley, W.L., Khain, A., Cotton, W.R., Carrión, G., Ginis, I., Golden, J.H., 2012. Aerosol effects on microstructure and intensity of tropical cyclones. *Bull. Am. Meteorol. Soc.* 93 (7):987–1001. <http://dx.doi.org/10.1175/BAMS-D-11-00147.1>.
- Sarkadi, N., Geresdi, I., Thompson, G., 2016. Numerical simulation of precipitation formation in the case orographically induced convective cloud: comparison of the results of bin and bulk microphysical schemes. *Atmos. Res.* 180:241–261. <http://dx.doi.org/10.1016/j.atmosres.2016.04.010>.
- Shen, X., Wang, Y., Li, X., 2011a. Radiative effects of water clouds on rainfall responses to the large-scale forcing during pre-summer heavy rainfall over southern China. *Atmos. Res.* 99:120–128. <http://dx.doi.org/10.1016/j.atmosres.2010.09.011>.
- Shen, X., Wang, Y., Li, X., 2011b. Effects of vertical wind shear and cloud radiative processes on responses of rainfall to the large-scale forcing during pre-summer heavy rainfall over southern China. *Q. J. R. Meteorol. Soc.* 137:236–249. <http://dx.doi.org/10.1002/qj.735>.
- Skamarock, W.C., Klemp, J.B., 2008. A time-split non-hydrostatic atmospheric model for weather research and forecasting applications. *J. Comput. Phys.* 227:3465–3485. <http://dx.doi.org/10.1016/j.jcp.2007.01.037>.
- Straka, J.M., Mansell, E.R., 2005. A bulk microphysics parameterization with multiple ice precipitation categories. *J. Appl. Meteorol.* 44:445–466. <http://dx.doi.org/10.1175/JAM2211.1>.
- Sui, C.-H., Li, X., Yang, M.-J., Huang, H.-L., 2005. Estimation of oceanic precipitation efficiency in cloud models. *J. Atmos. Sci.* 62:4358–4370. <http://dx.doi.org/10.1175/JAS3587.1>.
- Tao, W.-K., Simpson, J., 1989. Modeling study of a tropical squall-type convective line. *J. Atmos. Sci.* 46:1777–202. [http://dx.doi.org/10.1175/1520-0469\(1989\)046<1777:MSOATS>2.0.CO;2](http://dx.doi.org/10.1175/1520-0469(1989)046<1777:MSOATS>2.0.CO;2).
- Tao, W.-K., Shi, J.J., Chen, S.S., Lang, S., Lin, P.-L., Hong, S.-Y., Peters-Lidard, C., Hou, A., 2011. The impact of microphysical schemes on hurricane intensity and track. *Asia-Pac. J. Atmos. Sci.* 47:1–16. <http://dx.doi.org/10.1007/s13143-011-1001-z>.
- Thompson, G., Rasmussen, R.M., Manning, K., 2004. Explicit forecasts of winter precipitation using an improved bulk microphysics scheme. Part I: description and sensitivity analysis. *Mon. Weather Rev.* 132:519–542. [http://dx.doi.org/10.1175/1520-0493\(2004\)132_0519:EFPWPU>2.0.CO;2](http://dx.doi.org/10.1175/1520-0493(2004)132_0519:EFPWPU>2.0.CO;2).
- Thompson, G., Field, P.R., Rasmussen, R.M., Hall, W.D., 2008. Explicit forecasts of winter precipitation using an improved bulk microphysics scheme. Part II: implementation of a new snow parameterization. *Mon. Weather Rev.* 136:5095–5155. <http://dx.doi.org/10.1175/2008MWR2387.1>.
- Wang, Y.Q., 2002. An explicit simulation of tropical cyclones with a triply nested movable mesh primitive equation model: TCM3. Part II: model refinements and sensitivity to cloud microphysics parameterization. *Mon. Weather Rev.* 130:3022–3036. [http://dx.doi.org/10.1175/1520-0493\(2002\)130_3022:AESTC>2.0.CO;2](http://dx.doi.org/10.1175/1520-0493(2002)130_3022:AESTC>2.0.CO;2).
- Wang, Y., Shen, X., Li, X., 2010. Microphysical and radiative effects of ice clouds on responses of rainfall to the large-scale forcing during pre-summer heavy rainfall over southern China. *Atmos. Res.* 97:35–46. <http://dx.doi.org/10.1016/j.atmosres.2010.03.005>.
- Yin, Y., Levin, Z., Reisin, T., Tzivion, S., 2000. The effects of giant cloud condensation nuclei on the development of precipitation in convective clouds – a numerical study. *Atmos. Res.* 53:91–116. [http://dx.doi.org/10.1016/S0169-8095\(99\)00046-0](http://dx.doi.org/10.1016/S0169-8095(99)00046-0).

- Zacharov, P., Řezáčová, D., 2009. Using the fractions skill score to assess the relationship between an ensemble QPF spread and skill. *Atmos. Res.* 94:684–693. <http://dx.doi.org/10.1016/j.atmosres.2009.03.004>.
- Zacharov, P., Řezáčová, D., Brožková, R., 2013. Evaluation of the QPF of convective flash flood rainfalls over the Czech territory in 2009. *Atmos. Res.* 131:95–107. <http://dx.doi.org/10.1016/j.atmosres.2013.03.007>.
- Zhang, D.-L., 1989. The effect of parameterized ice microphysics on the simulation of vortex circulation with a mesoscale hydrostatic model. *Tellus* 41A:132–147. <http://dx.doi.org/10.1111/j.1600-0870.1989.tb00394.x>.
- Zhu, T., Zhang, D.L., 2006. Numerical simulation of Hurricane Bonnie (1998). Part II: sensitivity to cloud microphysical processes. *J. Atmos. Sci.* 63:109–126. <http://dx.doi.org/10.1175/JAS3599.1>.